Polish Journal of Medical Physics and Engineering
The Journal of Polish Society of Medical Physics
ISSN 1898-0309, doi: 10.2478/pjmpe-2025-0014

June 2025
Vol 31, Issue 2

Scientific Paper

Evaluation of dose calculation accuracy within temporary breast tissue expanders with integrated/remote metallic ports

Aleksandra Bochyńska [1,ABCDEF,*], Anna Zawadzka [1,ABCDEF], Agnieszka Walewska [1,ABCDEF], Magdalena Dobrzyńska [2,CF], Pawel Kukołowicz [1,CDEF]

[1]*Department of Medical Physics, The Maria Sklodowska-Curie National Research Institute of Oncology, W. K Roentgena 5 Street, Warsaw, Poland*
[2]*Particle Acceleration Physics and Technology Division, National Centre for Nuclear Research, A. Sołtana 7 Street, Otwock, Świerk, Poland*
**Corresponding author: Aleksandra Bochyńska; aleksandra.bochynska@nio.gov.pl*

(received 4 November 2024; revised 10 January 2025; accepted 16 April 2025)

Abstract

Purpose: To investigate the dose calculation accuracy of the Eclipse TPS in the presence of temporary breast tissue expanders with high-density metallic ports.

Materials and Methods: Four anthropomorphic phantoms were prepared, with integrated Nagor (F_I^N) and Mentor metallic ports (F_I^M), remote Mentor port (F_R^M) and reference one without high-density materials (F^R). For each phantom, 16-bit CTs were performed, and several treatment plans (3D, VMAT) were prepared in the Eclipse TPS. X6FF, X15FF and X6FFF and two dose calculation algorithms (AAA, AXB) were used. Two calibration curves (CalC) were used to calculate the dose: standard and extended (with higher material densities added). The calculation and film measurements were compared. Differences in the dose distributions obtained for both CalC were analyzed.

Results: For F^R, differences below 5% were obtained for 95% of all measurement points (mean -0.1 ± 2.5%), whereas for phantoms with ports, the differences were 90% (F_I^N), 91% (F_I^M) and 93% (F_R^M). For F_I^N and F_I^M only at one point close to the port (no. 3), a significantly greater difference was observed (9.2%). The beam energy and calculation algorithm do not seem to impact the results. When comparing calculations for standard and extended CalC, dose differences were more pronounced for the 3D technique than for the VMAT technique.

Conclusions: The calculation algorithm and beam energy do not seem to impact the results when appropriate CT parameters and the extended CalC are implemented. A slightly higher dose is measured at the surface of the phantom, although this appears to also apply to points away from the ports. VMAT appears to be less sensitive to errors.

Keywords: *tissue breast expander, treatment planning system, dose calculation accuracy, metallic port*

1. Introduction

More than one-third of women diagnosed with early-stage breast cancer choose mastectomy as their primary treatment method, which can be followed by breast reconstruction.[1] However, considering the influence of postmastectomy radiotherapy (PMRT), an increasing number of centers choose to perform delayed–immediate reconstruction, where a temporary tissue expander (TTE) is placed during surgery.[2,3] TTE allows the overlying skin to stretch and expand, making space for permanent implant exchange after receiving PMRT.[4] At our institution, the expanders are gradually filled with saline solution injected through the port with magnetic properties that facilitate accurate needle insertion.[2] In expanders with integrated ports, the metal port is located on the expander surface in the nipple area. For distal expanders, a remote port located in the armpit area is connected to the expander by a flexible filling tube.

Naoum et al.[5] and Sekiguchi et al.[6] reported a possible increased risk of complications and poor cosmetic results in a group receiving postmastectomy radiotherapy to the TTE compared with the permanent implant. The presence of the material certainly affects the dose distribution in the area close to the port.[4] However, assessing the impact of high-Z materials on dose distribution remains a challenge. Artifacts caused by the metal parts of TTEs degrade the CT image quality, making the dose distribution calculation less precise.[7] The solution used in modern CT scanners to improve image quality is the implementation of metal artifact reduction (MAR) algorithms. These algorithms correct the raw projection data via projection-based methods and reconstruct the improved data set based on a new, modified sinogram.[8] Using MAR algorithms alone is not enough since, in typical 12-bit images, the CT scale saturates at 3 071 Hounsfield Units (HUs), which is insufficient when imaging the metal parts of TTEs. In this

Authors' contribution: A – Research concept and design, B – Collection and/or assembly of data, C – Data analysis and interpretation, D – Writing the article, E – Critical revision of the article, F – Final approval of the article.

case, it is necessary to extend the bit depth of CT and reconstruct images in 16-bit CT format (with values up to 65 535 HU).[8,9] Extending the calibration curve is another element necessary to enable calculations for materials with HU densities greater than 3 071 HU in the treatment planning system (TPS). The calibration curve converts HU to electron density (or mass density) relative to water. It typically has a standard human tissue range from approximately -900 HU for the lungs to approximately 3 000 HU for dense bones.[10] Therefore, when metal elements are included in dose calculations, extending the standard range is crucial to achieve more accurate results.

In this study, we investigated the dose calculation accuracy of Eclipse TPS v.15.6 (Varian Medical Systems, Palo Alto, CA, USA) in the presence of high atomic number elements for postmastectomy patients with tissue expanders. We tested the Acuros XB (AXB) calculation algorithm with the HU-to-mass density calibration curve and the Anisotropic Analytical Algorithm (AAA) with the HU-to-electron density relative to water calibration curve. We analyzed the influence of the implemented calibration curve, irradiation technique, calculation algorithm, and photon beam energy on the accuracy of the calculated dose distribution. To our knowledge, this is the first study considering all those aspects.

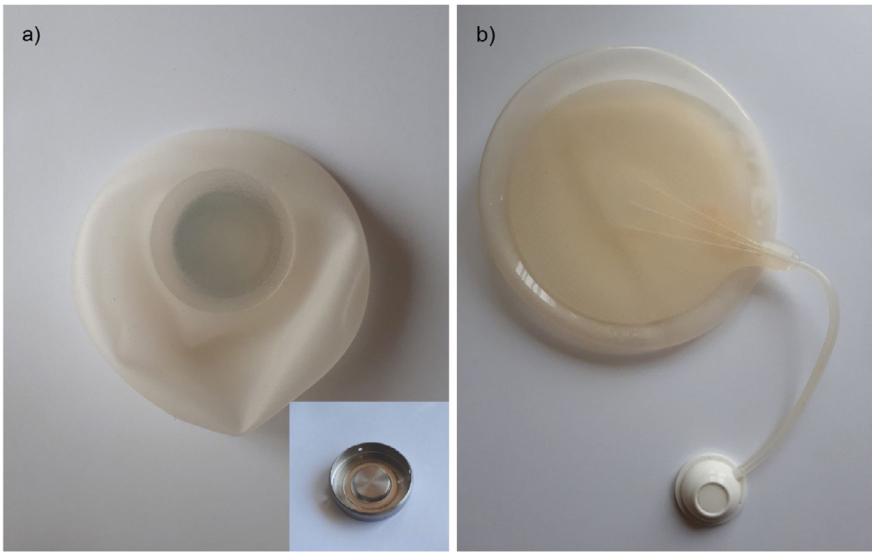

Figure 1. a) Expander with integrated port (Nagor); bottom right corner: extracted port. b) Expander with a remote port (Mentor). Both expanders before filling with saline solution.

2. Materials and methods

2.1. Expanders

Two breast tissue expanders with integrated ports were used: Mentor (Mentor Worldwide LLC, Santa Barbara, CA, USA), and Nagor (GC Aesthetics, Dublin, Ireland) and one with a remote port (Mentor) (**Figure 1**). Each expander had a volume of 400 cm^3. The integrated Mentor port includes a SmCo5 magnet (Samarium-Cobalt, density 8.2–8.5 g/cm^3), measuring 1.27 cm in diameter and 0.48 cm thick.[11] For the integrated Nagor port and the remote Mentor, the company's brochures lack complete information on the materials they are made of.

2.2. Phantoms

To investigate the influence of port presence on the calculated dose distribution, four anthropomorphic breast phantoms were made from paraffin wax (**Figure 2**): a phantom without any expander or metallic elements (F^R), two phantoms with integrated expanders (F_I^N – Nagor, F_I^M – Mentor), and one phantom in which only the remote port without an expander was placed (F_R^M – Mentor). Expanders with integrated ports were filled according to the patients' procedures. Despite this, some air remained in the expanders, as shown in **Figure 2a**.

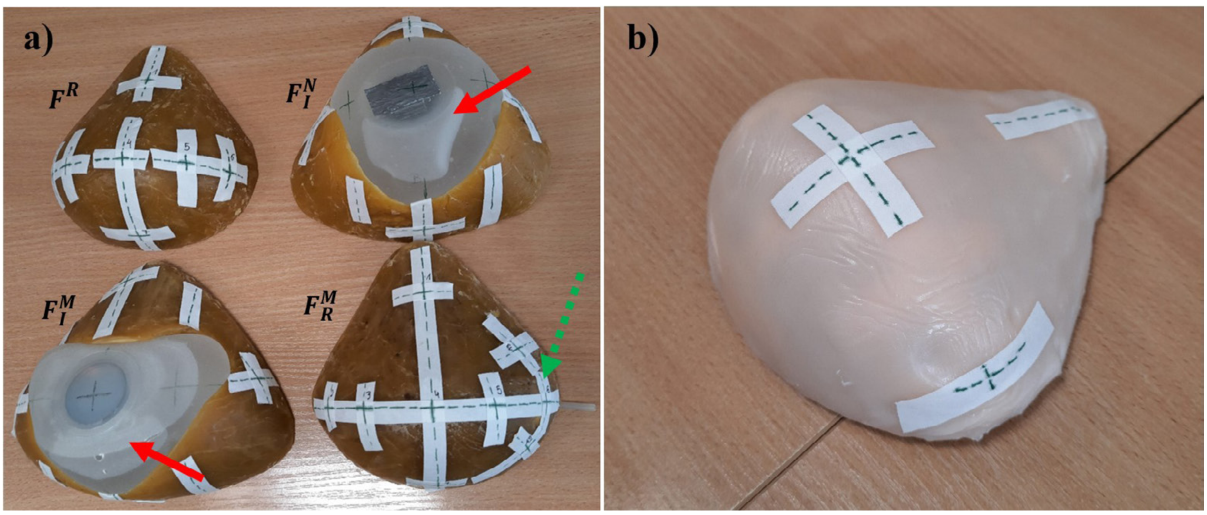

Figure 2. a) Breast phantoms: phantom without an expander FR, phantoms with integrated expanders: F_I^N and F_I^M, phantom with a remote port F_R^M. The red arrows indicate the air volume. The green dotted arrow points to the position of the remote port. b) Example of one of the phantoms covered with a thermoplastic bolus.

The remote port in the phantom simulated its clinical location in the patient (green dotted arrow in **Figure 2a**). For the remote port-only case, only the port cut off from the expander, not the expander itself, was embedded in the phantom. Each phantom was covered with a 5 mm thermoplastic bolus to simulate clinical situations when an implant is placed under the skin or muscle.

Based on the results (differences between calculations and measurements) obtained for F^R, the acceptance limit for the differences obtained for phantoms with ports was determined.

2.3. CT scan of phantoms

The phantoms were placed on 5 cm polystyrene, water-equivalent slabs (30 × 30 × 1 cm, density of 1.04 g/cm^3) and scanned with a Discovery RT CT scanner (GE Healthcare, Chicago, Illinois, USA). A breast scanning protocol (120 kVp, 1.25 mm slice thickness) routinely used in the clinic was used. The proposed setup did not simulate the patient's anatomy (lungs and chest wall), but these structures have a negligible influence on the dose distribution on the surface (skin).

To reduce artifacts caused by metallic ports, the projection-based Smart Metal Artifact Reduction (MAR) method and an extended (16-bit) CT scale were used. However, despite MAR correction, for expanders with integrated ports, some artifacts around the ports remained visible on the CT images (**Figure 3a**). Since the artifacts were minor and not located close to the measurement points, it was decided not to overwrite their density.

The exterior outline included a bolus-covered breast phantom and slabs. The integrated ports were manually contoured as high-resolution structures via bone window thresholding. **Figure 3b** presents the hand-contoured Mentor integrated port. The remote port was also contoured in the same way. The HU values of the ports were analyzed on the basis of the delineated contours. The dimensions of the integrated ports (diameter and height) obtained from the CT images were compared with the size determined with a caliper.

The planning target volume (PTV) for all phantoms was defined as a breast phantom with a margin of 5 mm, including a bolus. In F_I^N and F_I^M, the expander was excluded from the PTV. For the F_R^M, the port was also included in the PTV.

2.4. Treatment plans

3D-conformal and volumetric–modulated arc therapy (VMAT) plans were prepared for each phantom in the Eclipse TPS v.15.6 (Varian Medical Systems, Palo Alto, CA, USA). Two lateral opposing fields with gantry angles of 80° and 280° were used in a static plan. Additionally, dynamic wedges were added for the X6FF and X15FF beams, and a gantry angle of 80˚ to improve plan homogeneity. For VMAT, the plan geometry was a single half-arc from 90° to 270° gantry angle and collimator angle of 0°. Dose calculations were performed for two algorithms: AAA (v.15.6.05) and beam energies X6FF, X15FF, X6FFF and AXB (v.15.6.03). For the AXB, the "dose-to-medium" dose reporting mode[12] and X6FFF beam were applied since only this energy is commissioned for clinical use. The prescription dose of 3 Gy was normalized to the mean dose to the PTV. For each VMAT plan, one optimization was performed with the same optimization constraints and number of iterations to maintain plan preparation consistency. This study aimed to evaluate the agreement between TPS calculations and measurements in the presence of high-Z materials, so we wanted to avoid additional variables such as plan modulation. The resulting plans were not considered clinically acceptable.

The dose calculation grid size was 1.25 mm, which was consistent with the CT slice thickness and default grid resolution used for the AXB algorithm. Plans were delivered on Varian machines: True Beam (MLC120, X6FF, X15FF, X6FFF) and EDGE (MLC HD120, X6FFF). Figs. 4a and 4b present the plan geometry. The parameters used are summarized in **Table 1**.

Table 1. Plans parameters (FF – flattening filter, FFF – flattening filter free)

Calculation algorithm	Linac	Photon beam	Technique	Calculation grid size
Analytical Anisotropic Algorithm (AAA)	TrueBeam (MLC 120)	6 MV FF 15 MV FF 6 MV FFF	3D VMAT	1.25 mm
Acuros XB dose-to-medium mode (AXB)	Edge (HD MLC)	6 MV FFF		

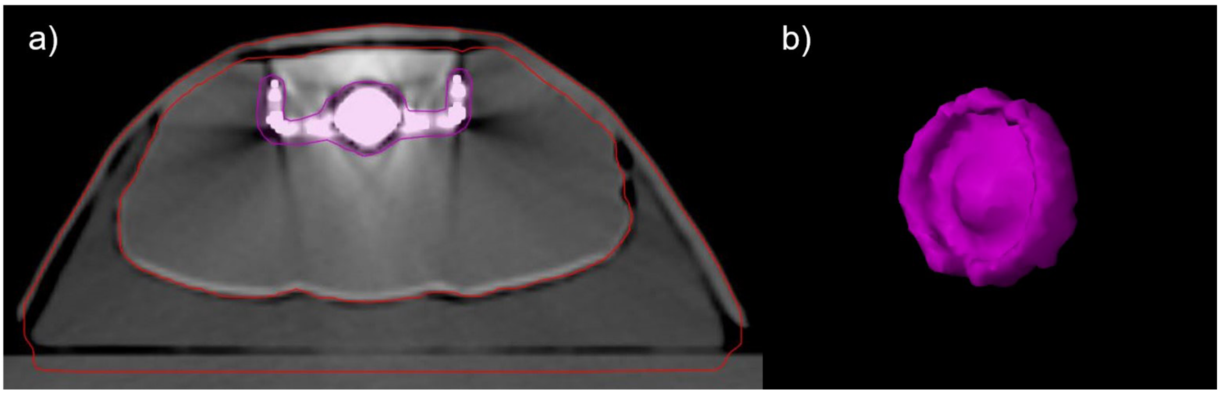

Figure 3. a) Transverse CT scan section of the F_I^N phantom showing the integrated port (purple) and PTV (red), b) 3D model of the integrated port.

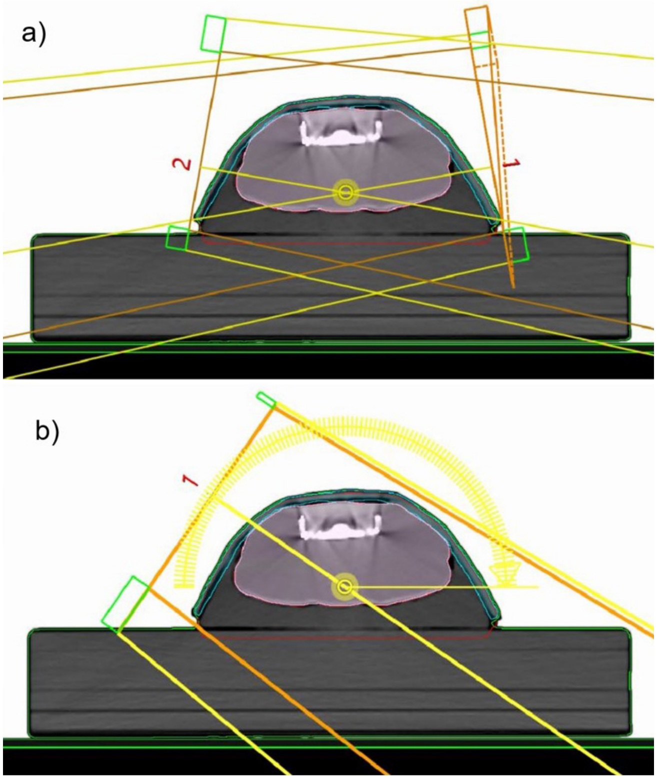

Figure 4. Transversal CT scan with a beam arrangement for a) 3D conformal and b) VMAT plans.

The extended CT calibration curve was used for dose calculations. The calibration curve converts HU to electron density (or mass density) relative to water. HUs are defined as $HU = 1000(\mu/\mu_w - 1)$, where μ and μ_w are the linear attenuation coefficients of the material and water, respectively. The standard approach was used for both algorithms to prepare extended calibration curves. The CIRS 062 M phantom with a set of tissue-equivalent materials and a titanium insert was scanned. The point corresponding to the density of steel was also added based on the averaged values taken from the literature. The maximum values for both the relative electron density and mass density calibration curves were 6.7 and 8.1 g/cm^3 (steel density) for the AAA and AXB algorithms, respectively. These values corresponded to 10 000 HU.

For AAA, if HU values found in CT images exceed the maximum value defined in the calibration curve, they are overwritten by this maximum HU value, and the corresponding electron density in the calculation is used. For the AXB algorithm, if HU outside the calibration curve appears and its volume is less than 1.0 cm^3 (the value is set by the user during the system configuration), the system assigns pixels with a mass density of 3.0 g/cm^3. For larger volumes, the appropriate material must be assigned. If the material is known, it is possible to select its density from a predefined library.[13] Based on CT information, volumes and mean HU values of areas with densities exceeding 3.0 g/cm^3 (port area) were 1.48 cm^3 and 10 292 HU for F_I^N and 1.16 cm^3 and 10 652 HU for F_I^M. These values were overwritten for dose calculation with steel parameters (9 943 HU, 8.1 g/cm^3). For the remote port, HU value assignment was not needed.

2.5. Measurements

During CT scanning, ten or eleven measurement points were marked on each phantom depending on the phantom type, as shown in **Figure 5**. At the top of the phantom, under the bolus, five measurement points (2-6) were placed at the port level. Three points (9, 10, 11) were placed under the expander: for F_I^N and F_I^M, between the expander and paraffin, and for F^R and F_R^M, between the phantom and the slab's surface. Two additional points (1, 7) were chosen at the phantom top, above and below the port level in the longitudinal direction. These were the points where inaccuracies due to high-Z materials should not affect the measurement results. The same applied to point 8 at the bottom of F^R and F_R^M.

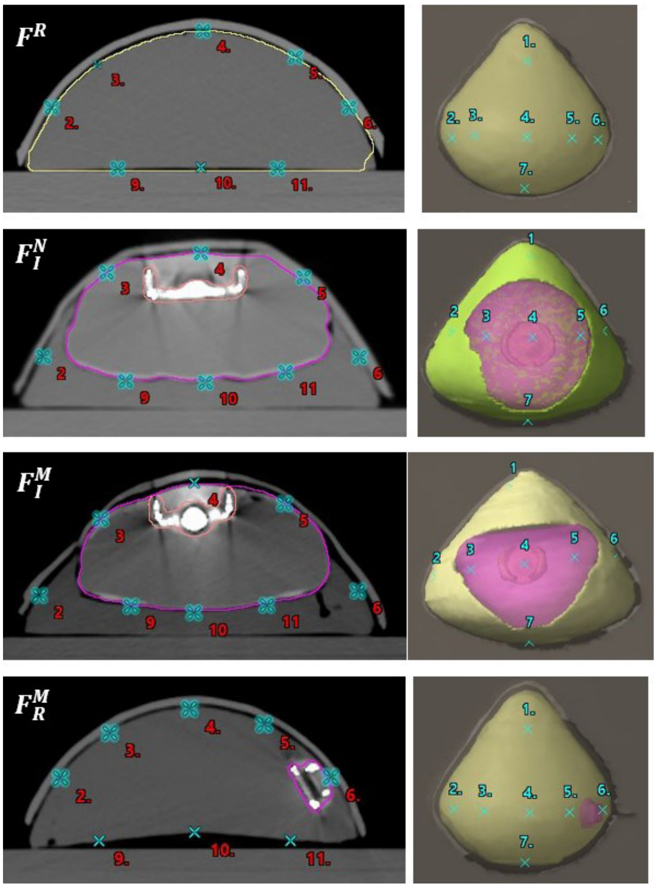

Figure 5. Placement of measurement points.

The calculations at these points were verified with Gafchromic EBT3 films (Ashland Advanced Materials, Bridgewater, NJ, USA).[14,15] During plan delivery, one film detector (1.5 × 1.5 cm^2) was placed at each point underneath the bolus or phantom (**Figure 5**).

Before each plan irradiation, cone-beam CT (CBCT) was performed to ensure accurate phantom and bolus positioning. The head protocol was used with the following parameters: full fan mode, 100 kVp, 270 mAs, and 0.25 cm slice thickness. T. Aland et al.[16] showed that the doses delivered when imaging with similar parameters are negligibly small (less than 2 cGy) and do not significantly affect the obtained results. The film calibration procedure was performed as described by D. Lewis et al.[17]. The films were scanned using an Epson Perfection V750 Pro scanner in three-channel (RGB), 48-bit (72 dpi) transmission mode.

Film scanning and data analysis were performed in Film QA Pro (Ashland software) according to the procedure described by D. Lewis et al.[17] and A. Micke et al.[18].

For each point, the percentage difference between the mean dose in the region of interest (ROI) measured and calculated by the TPS was calculated:

$$D_{diff}\left[\%\right]=\frac{D_{TPS}-D_{measured}}{D_{measured}}\cdot 100\% \quad (1)$$

Python-based in-house software "ROI" was used to obtain dose-in-point or ROI data from the indicated DICOM files from Eclipse TPS, as it was impossible to obtain ROI data directly from TPS.

The standard deviation (SD) for points of the F^R phantom was calculated. For phantoms with metal ports, differences between calculations and measurements of less than two SDs of the reference phantom were considered acceptable.

The differences between the measurements and calculations in the presence of high-Z materials were analyzed. Whether they depended on energy, plan geometry, point position relative to the port or computational algorithm was checked.

2.6. Phantom and film position reproducibility

The influence of the reproducibility of phantom and film positioning on dose measurement was evaluated. Three measurements of the same 3D conformal and VMAT plan (X6FFF, TrueBeam) were performed for the F_I^N and F^R phantoms. Before each plan was measured, the films and phantom were repositioned according to the established procedure based on CBCT imaging. A standard deviation normalized to the mean value of the results was determined for each measurement point.

2.7. Comparison of dose distributions for standard and extended calibration curves

The impact of the extended CT calibration curve on dose calculations was investigated. Plans were recalculated for extended and standard CT calibration curves and compared by subtracting dose distributions. Differences in dose distributions were evaluated.

2.8. Statistical analysis

To verify the normality of the data distribution, the Shapiro–Wilk test was conducted. A two-sample t test was used to determine any statistically significant differences between the results obtained for each phantom and the analogous situation for the F^R phantom. Tests with a significance level of $\alpha = 0.05$ and a 95% acceptance range were conducted.

When the influence of the dose calculation algorithm was compared, the Wilcoxon signed-rank test was performed, with the significance level defined as $\alpha = 0.05$. Differences were considered statistically significant when $p \leq 0.05$. This means that the results obtained for a particular combination of expander, energy, and algorithm differed from those observed in the corresponding situation with the reference phantom (without the expander), indicating that the expander has a significant impact on the dose distribution.

3. Results

3.1. CT scan of phantoms

Table 2 shows the maximum, mean and standard deviation HU values obtained for all types of ports. In all the cases, the maximum HU values exceeded the maximum value of the standard HU scale (3 071 HU). However, the maximum HU value for the remote port was almost four and a half times lower than that for the integrated ones, indicating that it was made of material with a lower atomic number. Even though the maximum HU values were very high, most voxels did not exceed 6 000 HU. However, only the remote port was within the saturation value of the 12-bit CT HU scale.

Table 2. Maximum, mean and standard deviation (SD) HU values for each port

Port type	Expander (phantom)		HU_{max}	$HU_{mean} \pm HU_{SD}$
Integrated	Mentor_I	(F_I^M)	23 709	1 708 ± 3 965
	Nagor	(F_I^N)	23 371	1 970 ± 4 051
Remote	Mentor_D	(F_R^M)	5 241	395 ± 899

The dimensions of the ports were also compared with their actual sizes determined with a caliper. For the integrated ports, the CT-determined dimensions were consistent with the real dimensions, with a diameter of 4.1 cm and a height of 1.0 cm. However, there were discrepancies in the thicknesses of the sidewalls of the ports. The reason is that they were too thin (1 mm) to be correctly reconstructed with a slice thickness of 1.25 mm. There were no such problems with the reconstruction of the remote port. Based on the measured integrated port sizes and maximum HU values, more voxels with high HU values and, therefore, higher mean HU values were expected. It seems that due to the voxel size, which for the applied field of view (50 cm) was 0.98 mm × 0.98 mm × 1.25 mm, it was impossible to obtain complete image information.

3.2. Measurements

Table 3 summarizes the percentage dose differences between the TPS calculations and measurements (Eq. (1)) for single points in all four phantoms. There are also means and SDs for points divided into phantoms, energy and dose calculation algorithms. The p value shows which results in the phantoms with the expander are significantly different from the reference phantom. The mean difference for all the techniques, energies and algorithms for F^R was -0.1 ± 2.5% [-6.3%; 5.7%]. The mean results for the remaining phantoms were -0.1 ± 3.3% (p = 0.970) for F_I^N, 0.1 ± 3.1% (p = 0.714) for F_I^M, and 0.7 ± 2.9% (p = 0.064) for F_R^M. **Figure 6a** shows a graphical representation of these results.

The results, depending on the irradiation technique used, for F^R were 0.3 ± 2.5% [-4.5%; 5.7%] and -0.4 ± 2.4% [-6.3%; 5.1%] for the 3D conformal and VMAT plans, respectively. Similar results were obtained for both phantoms with integrated ports. For F_I^N it was on average -0.4 ± 3.4% (p = 0.325) for 3D conformal plans and 0.2 ± 3.3% (p = 0.327) for VMAT

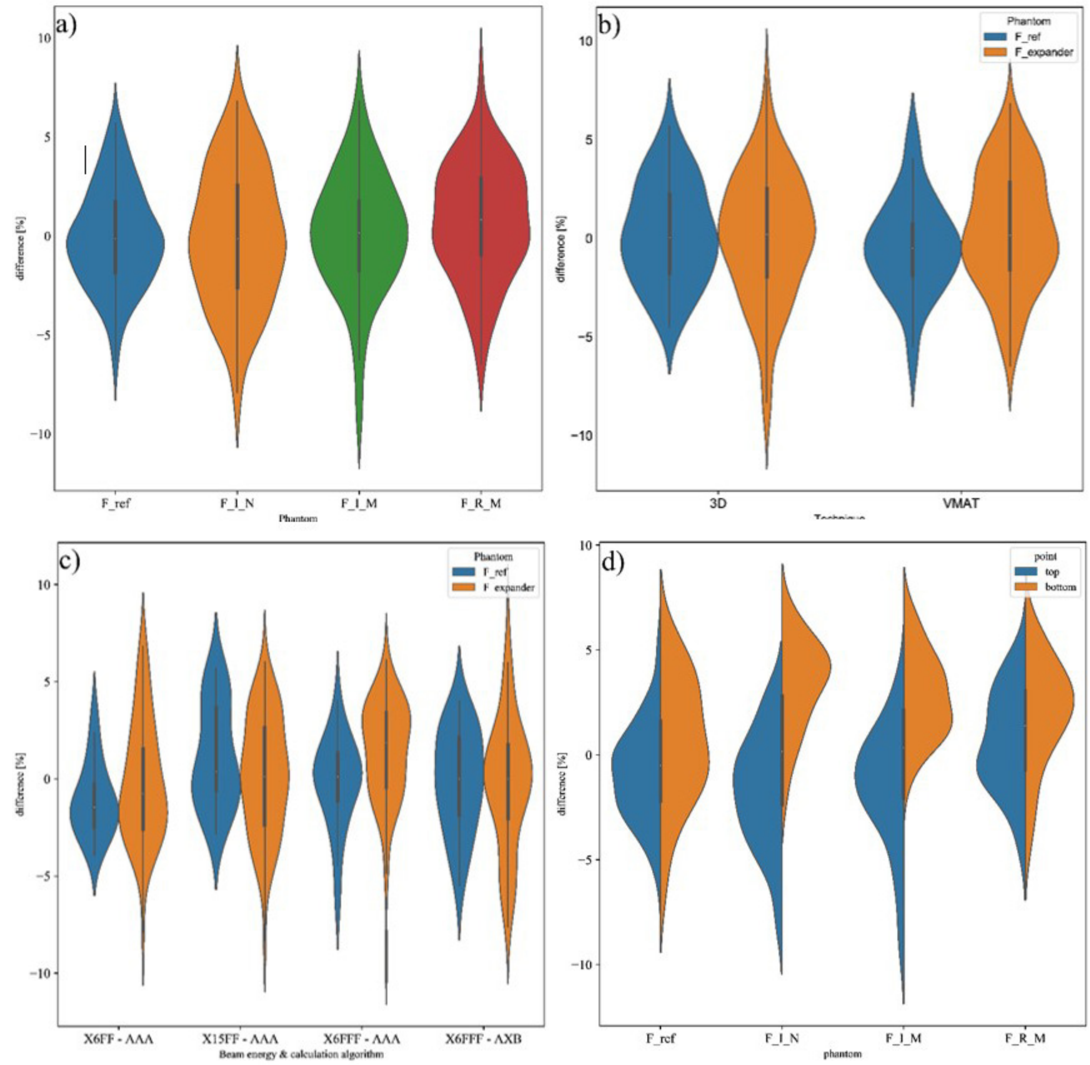

Figure 6. Comparison of obtained differences between calculations and measurements with division into a) phantoms, b) techniques, c) algorithms and energies, and d) measurement point locations. Top: points 2–6 for all phantoms. Bottom: 9 - 11 for F^R and F_R^N, 8-10 for F_I^M and F_I^N . F_ref - phantom without expander, F_expander – all phantoms with expanders. (*Violin plots were plotted at https://www.bioinformatics.com.cn/en, a free online platform for data analysis and visualization*).

plans. For F_I^M: -0.3 ± 3.2% (p = 0.339) for 3D conformal and 0.5 ± 2.9% (p = 0.115) for VMAT. Slightly worse but still not statistically significant results were obtained for F_R^M, where for 3D conformal and VMAT the mean values were 0.9 ± 3.0% (p = 0.405) and 0.6 ± 2.8% (p = 0.073), respectively. **Figure 6b** shows the differences obtained for both the 3D conformal and VMAT techniques summed for all phantoms with ports compared with the F^R phantom.

For F^R, the mean differences between the TPS calculations and film measurements by techniques, energies, and algorithms were between [-1.4%; 1.3%] and the maximum SD was equal to 3% (measurement combination: X15FF, AAA, 3D conformal). Comparing phantoms with ports, the lowest SD, equal to 1.1%, was obtained for F_R^M(X6FF, AAA and VMAT). At the same time, the highest SD of 4.2% was also obtained for F_R^M and the measurement combination X6FFF, AXB and VMAT. When comparing the results with F^R, for F_I^M and F_I^N, the mean difference was outside the range of ± 1.4% for 3 cases only. However, in contrast, the SDs were greater than 3% for 5 out of 8 for F_I^N and for 3 (all 3D conformal plans) out of 8 for F_I^M.

In four cases (**Table 3**), the difference between the analyzed phantom and the F^R phantom could be considered statistically significant (p < 0.05). Two of them occurred for the F_R^M phantom, the AAA algorithm and the X6FFF beam (both for 3D conformal and VMAT plans), and the other two included the X6FF beam and VMAT plans (F_I^N and F_I^M phantoms).

When phantoms with only ports were analyzed, the smallest differences were observed for the AAA algorithm and flattened energies (X6FF, X15FF). The means were -0.2 ± 3.1% [-7.9%; 6.8%] (p = 0.180) and 0.1 ± 3.0% [-8.3%; 6.0%] (p = 0.184) for X6 FF and X15 FF, respectively. The worst agreement was reported for X6FFF and AAA (mean 1.3 ± 2.7%, [-9.2%; 6.1%] (p = 0.015). For the AXB, the mean difference was -0.3 ± 3.3% [-7.6%; 8.1%] (p = 0.712). **Figure 6c** compares the F^R phantom and phantoms with ports, divided into energies and algorithms.

For F^R, at 95% of all measurement points, the differences were less than 5%. For phantoms with ports, the differences below 5% were, respectively, in 90% for F_I^N, 91% for F_I^M, and 93% for the F_R^M measurement points (**Table 4**). The largest

Table 3. Percentage dose differences [%] (calculated according to Eq. 1.) for single points between TPS calculations and measurements for phantom without expander F^R, phantoms with integrated ports: F_I^N and F_I^M and phantom with remote port F_R^M. Points located at the bottom of the expander/phantom were separated. P values show if the differences are statistically different from reference phantom results. Points close to the metal port were marked (light grey). Dark grey cells highlight points where the dose difference exceeded 5%. alg. – calculation algorithm.

		alg.	energy	point no.												
						top					bottom					
				1	2	3	4	5	6	7	8	9	10	11	mean±SD	p
F^R[%]	3D	AAA	X15 FF	-2.1	3.1	-1.5	-0.5	0.4	-0.8	-2.3	4.0	3.9	**5.7**	4.8	**1.3 ± 3.0**	
			X6 FF	-0.9	-2.4	-3.9	0.2	-2.5	-3.8	-0.8	1.0	-1.7	1.2	3.5	**-0.9 ± 2.3**	
			X6 FFF	0.0	-2.2	-2.5	1.8	0.0	-4.5	0.2	2.5	-0.2	0.6	1.6	**-0.2 ± 2.1**	
		AXB	X6 FFF	2.7	0.0	-2.3	2.0	-0.1	-3.7	-1.0	3.1	2.6	4.0	2.2	**0.9 ± 2.5**	
	VMAT	AAA	X15 FF	5.0	1.7	2.1	-0.2	**5.1**	0.4	-2.8	1.1	-0.6	-0.5	-0.5	**1.0 ± 2.4**	
			X6 FF	-1.8	-2.7	-3.0	-1.2	-1.5	-2.7	-1.4	-0.1	-2.1	-1.0	2.4	**-1.4 ± 1.5**	
			X6 FFF	-0.2	-0.5	0.3	1.8	0.4	-2.6	0.2	2.0	**-6.3**	-1.4	4.0	**-0.2 ±2.7**	
		AXB	X6 FFF	1.6	**-5.5**	-1.4	-2.0	0.2	0.0	0.6	2.7	-3.9	-3.1	-0.8	**-1.1 ±2.5**	
F_I^N [%]	3D	AAA	X15 FF	-3.9	0.6	-3.0	-2.9	1.1	0.3	-4.7	-	4.3	**6.0**	4.1	**0.2 ± 3.8**	
			X6 FF	-0.6	-3.9	**-7.9**	-3.7	-4.0	**-5.1**	-2.6	-	2.5	2.8	1.5	**-2.1 ± 3.5**	
			X6 FFF	2.8	-1.5	-2.1	2.6	-1.6	-1.5	0.1	-	3.7	**6.1**	4.1	**1.3 ± 2.9**	
		AXB	X6 FFF	0.2	0.2	**-7.6**	-0.3	-4.9	-0.6	0.3	-	0.0	2.1	0.9	**-1.0 ± 3.0**	
	VMAT	AAA	X15 FF	-2.7	-0.8	-4.9	-2.6	-0.4	-3.5	-5.0	-	3.7	4.1	4.8	**-0.7 ± 3.7**	
			X6 FF	1.6	0.6	-2.6	-0.4	-1.6	-2.3	-1.4	-	3.5	4.7	**6.8**	**0.9 ± 3.2**	**≤ 0.05**
			X6 FFF	1.8	0.4	-0.6	2.3	2.6	-0.8	-0.7	-	4.6	**5.1**	5.0	**2.0 ± 2.4**	
		AXB	X6 FFF	-1.2	**-5.2**	-3.0	2.7	2.8	-4.2	-4.9	-	-1.9	0.1	1.8	**-1.3 ± 3.1**	
F_I^M [%]	3D	AAA	X15 FF	-1.9	2.7	**-8.3**	-2.7	-2.4	0.6	-3.5	-	1.5	4.1	2.6	**-0.7 ± 3.7**	
			X6 FF	1.6	0.6	-2.6	-0.4	-1.6	-2.3	-1.4	-	3.5	4.7	**6.8**	**0.9 ± 3.2**	
			X6 FFF	1.0	-1.7	**-9.2**	-0.6	-4.9	-0.6	0.2	-	1.4	2.7	0.1	**-1.2 ± 3.5**	
		AXB	X6 FFF	-0.8	-0.3	**-6.2**	0.6	-1.0	-0.5	0.2	-	0.8	1.4	2.0	**-0.4 ± 2.3**	
	VMAT	AAA	X15 FF	-0.3	1.0	-4.5	0.1	-2.1	-0.3	-3.2	-	1.7	3.7	3.3	**-0.1 ± 2.6**	
			X6 FF	2.4	1.4	-2.7	2.9	0.0	1.5	3.7	-	**5.6**	**6.2**	4.9	**2.6 ± 2.7**	**≤ 0.05**
			X6 FFF	3.2	-2.3	-4.4	3.5	-1.6	0.5	-0.7	-	1.3	3.8	3.8	**0.7 ± 2.9**	
		AXB	X6 FFF	-1.6	-2.2	**-6.1**	-0.3	-2.1	-2.1	1.5	-	-1.0	0.6	1.1	**-1.2 ± 2.2**	
F_R^M [%]	3D	AAA	X15 FF	-2.5	2.5	-1.3	-0.1	0.8	4.7	-0.2	4.2	1.4	3.3	4.2	**1.6 ± 2.4**	
			X6 FF	-3.2	-3.8	-2.6	-1.2	-2.9	-1.6	-3.3	0.9	-4.2	-0.5	2.2	**-1.8 ± 2.0**	
			X6 FFF	0.0	1.0	1.9	4.0	2.5	0.2	3.0	2.2	2.7	3.4	2.9	**2.2 ± 1.3**	**≤ 0.05**
		AXB	X6 FFF	**-6.1**	0.1	-0.1	5.0	2.6	1.9	**8.1**	-4.4	4.8	3.1	2.5	**1.6 ± 4.1**	
	VMAT	AAA	X15 FF	-1.8	1.8	-0.4	-0.8	3.1	-0.7	0.1	0.4	1.1	2.7	-0.1	**0.5 ± 1.5**	
			X6 FF	-3.1	-0.9	-2.1	-1.4	-1.0	-0.6	-0.6	-0.9	-2.0	0.9	-2.5	**-1.3 ± 1.1**	
			X6 FFF	0.2	3.4	3.6	4.3	2.3	3.4	4.0	0.2	1.4	4.4	3.3	**2.8 ± 1.5**	**≤ 0.05**
		AXB	X6 FFF	**-6.5**	-0.6	-4.7	-0.8	0.8	1.6	1.9	-4.2	**6.0**	**5.3**	**5.3**	**0.4 ± 4.2**	

Table 4. Comparison of results for reference phantoms (F^R) and all phantoms with ports (F_I^N, F_I^M, F_R^M). Per cent and number of measurement points with dose difference ≤ 5% divided into a phantom, irradiation technique, beam energy, and calculation algorithm.

Phantom			
F^R	F_I^N	F_I^M	F_R^M
95% (84/88)	90% (72/80)	91% (73/80)	93% (82/88)

Irradiation technique		
	3D	VMAT
F^R	98% (43/44)	93% (41/44)
F_I^N, F_I^M, F_R^M	91% (113/124)	92% (114/124)

Beam energy & calculation algorithm				
	X6 AAA	X15 AAA	X6FFF AAA	X6FFF AXB
F^R	100% (22/22)	91% (20/22)	95% (21/22)	95% (21/22)
F_I^N, F_I^M, F_R^M	90% (56/62)	97% (60/62)	90% (56/62)	84% (52/62)

discrepancies (even greater than 7%) were observed mainly for phantoms with integrated ports and point 3 (**Figure 5**). A difference depending on the point location was also observed for these fantoms. The measured dose was higher than the calculated dose for points at the top of the port area (mean - 1.6%). Moreover, the mean difference was 3.1% for points at the bottom. **Figure 6d** shows the differences between points at the top and bottom, at ports areas for all the phantoms. Significant differences (above 5.3%) were noted for phantom F_R^M, the AXB, VMAT and points 9 - 11. The reason may be the air gap that occurred in the F_R^M fantom between the tabletop and the bottom of the phantom, reaching up to 6 mm. This resulted from the concavity of the base of the phantom, which formed during the paraffin cooling process. This air gap could have resulted in several unfavorable factors that influenced the obtained differences: 1) in-accurate adhesion of the films to the phantom (measurement error) and 2) algorithm calculation error at the boundary of highly different densities (system error). In addition, this area was within the dose gradient.

The results obtained for different beam energies and exposure techniques indicate that the differences in the highest values occurred for the 3D conformal technique, regardless of the energy. The calculation algorithm seemed to have no impact on the results. The difference in agreement within 5% for X6FFF (90% for AAA vs. 84% for AXB) seemed to be due to the three measurement points at the bottom of the F_R^M phantom. The measurement point location seemed to be the most crucial factor.

3.3. Phantom and film positioning reproducibility

The influence of phantom and film positioning on dose measurement reproducibility was verified according to the method described in subsection 2.6. The uncertainty of F^R positioning was on average 1.1% for the 3D conformal plan and 0.8% for the VMAT plan. The F_I^N values were 0.6% and 0.9%, respectively. This result indicated very good repeatability of the phantoms, expanders, and film detector positioning during the measurements.

3.4. Comparison of dose distributions for standard and extended calibration curves

Figure 7 shows the difference between the dose distributions for the 3D conformal and VMAT plans calculated with standard and extended calibration curves (X6FF, F_I^M). The X6FF beam energy was chosen as an example because it is the standard energy used to treat breast cancer patients at our center. Regardless of the treatment technique, differences in dose distribution occurred only for phantoms with integrated ports. The tangential field technique was associated with clearly visible dose attenuation behind the port. This resulted in a dose reduction in the shadow of the port, both in the volume of the expander and in a small part of the volume of the PTV.

For VMAT, the differences were more blurred and occurred mainly in the expander volume, which is not therapeutically relevant. The differences did not exceed 0.3 Gy (10% of the prescribed dose) for both integrated ports and treatment techniques. The second region of difference was the bolus mimicking the patient's skin. These differences may be due to inaccuracies in the TPS calculation algorithms occurring at shallow depths[19], as they were also visible in the regions outside of ports but also because of the different values of the electron density of artifacts visible in the CT image resulting from the use of different calibration curves.

For F_R^M, calculation point differences (less than 0.4 Gy) in the metal part of the port were observed only, and the calibration curve extension did not significantly affect the TPS calculation. Due to the small volume of high atomic number material, the difference in the calibration curves did not appear to be the source of the dose differences.

4. Discussion

In this study, we investigated the influence of three temporary tissue expanders with metallic ports on the dose calculation accuracy of the Eclipse TPS. TTEs may be a source of dose perturbation, leading to inaccuracies in dose calculations and, consequently, to local failure or undesirable side effects.

The number of breast cancer patients undergoing simultaneous mastectomy and reconstruction is currently increasing. Often, delayed–immediate reconstructions are chosen, where a TTE is placed during the surgery. However, while convenient for patients, the metallic elements included in TTE may induce several problems if radiotherapy is needed. Dedicated metal artifact correction algorithms improve image quality, but the accuracy of the calculations still needs to be verified before their first clinical use. In regard to calculations, there are two main sources of uncertainty. Several studies presented underdosage in the PTV region caused by port attenuation or unnecessary dose increase as an effect of secondary electron generation, which the TPS does not adequately model. The latter, however, may not be clinically meaningful. Trombetta et al.[20] showed that secondary electrons do not affect the dose distribution in the PTV due to their short range. Nevertheless, the proper dose attenuation behind the port should be validated.

Thompson et al.[21] showed that the dose reduction for a single field could reach 30% when a single X6 beam is used. Based on film measurements, Asena et al.[22] showed that magnetic disks reduce the average dose by approximately 20% for X6 and tangential fields. Moreover, they showed that the silicone elastomer shell of the Mentor implant also affects the dose distribution, reducing it by as much as 8%. However, in actual clinical situations, less underdosage was reported. Gee et al.[4]

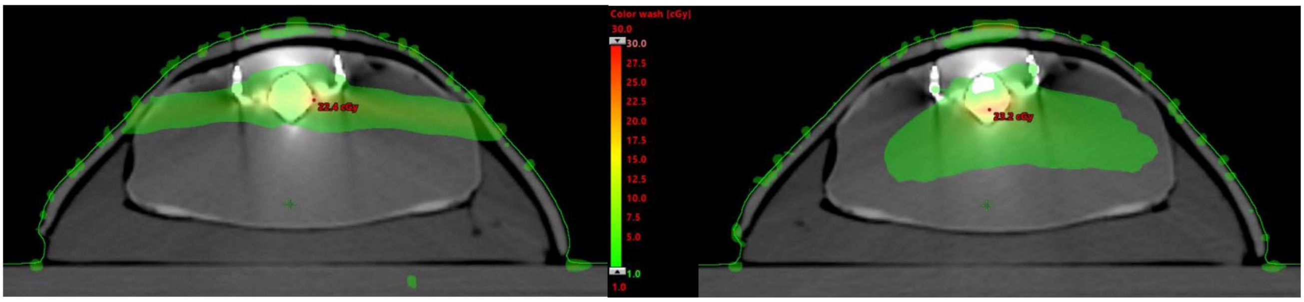

Figure 7. Dose distribution differences for the 3D conformal plan (left) and VMAT (right) for the F_I^M phantom. Range: 0.01 Gy–0.3 cGy, prescribed dose: 3 Gy.

based on film in vivo dosimetry, showed a regular dose reduction to the skin (mean of 7%) in the area shaded by the metal port when static tangential beams and the AAA algorithm were used. In this case, the metal artifact correction algorithm was not used, and ports were defined with artificially given HU numbers. Monte Carlo simulations conducted by Chatzigiannis et al.[23] show similar results: the presence of a metal port can result in a dose reduction of approximately 7% - 13% (X6) and 6% (X18) for tangential beams compared with the situation without an expander. In our study, an underdose at a similar level (10%) in a port shadow occurred if the correct calibration curve with extended HU values was not defined. The effect was more visible for two opposing fields.

The orientation of the port relative to the beam direction also plays an important role in the magnitude of dose reduction. Damast et al.[24] reported an underdosage in the phantom for a single field of 6% and 22% for the parallel and perpendicular port positions, respectively. Therefore, the influence of the port on the dose distribution may be more pronounced for static techniques than for dynamic ones. In 3D, the ports are often oriented in a direction close to parallel to the direction of the beam. In contrast, the VMAT technique delivers the dose from different directions, and the effect may be averaged. Park et al.[25] compared various radiotherapy techniques for breast cancer patients with Mentor TTE, Eclipse TPS, X6 beam energy and the AAA algorithm. They reported differences from 5.6% to 6.8% near the metal port for tangential fields. Yoon et al.[26] confirmed that the dose reduction effect was less significant for dynamic fields delivered from different directions. In our study, the difference between the dose calculations and measurements for both techniques was not as clear. However, more extreme values occurred with the 3D technique. When comparing the port types, the worst results were unexpectedly obtained for a remote port. The average difference between the calculated and measured doses reached 2.8%. However, less consistent results were obtained for F_I^N, where the maximum SD was 3.8%. Another analyzed parameter was the dose calculation algorithm. AAA is based on convolution and superposition of dose kernels scaled by medium density. AXB is a more advanced algorithm that uses the linear Boltzmann transport equation to calculate the interactions of radiation with matter and energy transport. [27] Cheng et al.[28], Ojala et al.[29] and Pawałowski et al.[30] reported better consistency between the measurements and calculations for the AXB algorithm than for the AAA near metallic materials. It was shown that for high-Z materials, compared with Monte Carlo simulations and measurements, the AAA algorithm overestimates the dose by up to 10%, whereas the AXB shows good agreement.[27] Our results stand in line with these conclusions. Despite worse agreement within 5% for the AXB (90% for the AAA vs. 84% for the AXB) when comparing all phantoms with ports, the mean difference was lower for the AXB (-0.3 ± 3.3% vs. 1.3 ± 2.7%; p = 0.027). The appearance of discrepancies between the measurement and AXB calculations may be due to the need to assign material from a predefined library to objects whose densities exceed 3.0 g/cm^3. In the case of breast tissue expander ports composed of several materials, selecting a single material with the proper density was very challenging, which could lead to calculation errors.

5. Conclusions

Our study shows that with proper preparation of all steps in radiotherapy treatment planning for patients with TTE, good accuracy in dose calculations can be achieved. The 16-bit CT images, metal artifact reduction algorithm and extended calibration curve enable good agreement between the calculations and measurements. Regardless of the technique, energy, and calculation algorithm, the difference between the calculations and measurements was smaller than 5% for most measurement points. However, when patients are irradiated with TTE implants, the VMAT technique appears to be less sensitive to errors. Our study shows that the calibration curve range is one of the most crucial factors affecting the accuracy of the calculation. If the calibration curve is restricted to tissue-equivalent materials, calculation errors can reach 10%. However, to demonstrate the real impact of the extended calibration curve on the dose calculation, it would be necessary to conduct a study on a larger group of clinical cases that considers actual clinical treatment plans. The implementation of the plans may vary for different patients, so future research should focus on dose analysis in both the PTV area and the organs at risk.

References

1. Ho AY, Hu ZI, Mehrara BJ, Wilkins EG. Radiotherapy in the setting of breast reconstruction: types, techniques, and timing. *Lancet Oncol*. 2017;18(12):e742-e753. doi:10.1016/S1470-2045(17)30617-4
2. Chen SA, Hiley C, Nickleach D, et al. Breast reconstruction and post-mastectomy radiation practice. *Radiation Oncology*. 2013;8(1). doi:10.1186/1748-717X-8-45
3. Manyam B V., Shah C, Woody NM, et al. Long-Term Outcomes After Autologous or Tissue Expander/Implant–Based Breast Reconstruction and Postmastectomy Radiation for Breast Cancer. *Pract Radiat Oncol*. 2019;9(6):e497-e505. doi:10.1016/j.prro.2019.06.008
4. Gee HE, Bignell F, Odgers D, et al. In vivo dosimetric impact of breast tissue expanders on post-mastectomy radiotherapy. *J Med Imaging Radiat Oncol*. 2016;60(1):138-145. doi:10.1111/1754-9485.12403
5. Naoum GE, Ioakeim MI, Shui AM, et al. Radiation Modality (Proton/Photon), Timing, and Complication Rates in Patients With Breast Cancer Receiving 2-Stages Expander/Implant Reconstruction. *Pract Radiat Oncol*. 2022;12(6):475-486. doi:https://doi.org/10.1016/j.prro.2022.05.017
6. Sekiguchi K, Kawamori J, Yamauchi H. Breast reconstruction and postmastectomy radiotherapy: complications by type and timing and other problems in radiation oncology. *Breast Cancer*. 2017;24(4):511-520. doi:10.1007/s12282-017-0754-3

7. Grams MP, Fong de los Santos LE, Antolak JA, et al. Cadaveric verification of the Eclipse AAA algorithm for spine SBRT treatments with titanium hardware. *Pract Radiat Oncol*. 2016;6(2):131-141. doi:10.1016/j.prro.2015.10.012
8. Glide-Hurst C, Chen D, Zhong H, Chetty IJ. Changes realized from extended bit-depth and metal artifact reduction in CT. *Med Phys*. 2013;40(6). doi:10.1118/1.4805102
9. Mullins JP, Grams MP, Herman MG, Brinkmann DH, Antolak JA. Treatment planning for metals using an extended CT number scale. *J Appl Clin Med Phys*. 2016;17(6):179-188. doi:10.1120/jacmp.v17i6.6153
10. Wathen CA, Foje N, van Avermaete T, et al. In vivo X-ray computed tomographic imaging of soft tissue with native, intravenous, or oral contrast. *Sensors (Switzerland)*. 2013;13(6):6957-6980. doi:10.3390/s130606957
11. Dinc S. Experimental and Monte Carlo evaluation of effects of temporary tissue expanders (TTE) on radiotherapy dose distribution. *Ann Med Res*. 2020;27(6):1533. doi:10.5455/annalsmedres.2019.12.800
12. Ma CM, Li J. Dose specification for radiation therapy: Dose to water or dose to medium? *Phys Med Biol*. 2011;56(10):3073-3089. doi:10.1088/0031-9155/56/10/012
13. Fogliata A, Nicolini G, Clivio A, Vanetti E, Cozzi L. Dosimetric evaluation of Acuros XB Advanced Dose Calculation algorithm in heterogeneous media. *Radiation Oncology*. 2011;6(1):82. doi:10.1186/1748-717X-6-82
14. Dąbrowski R, Drozdyk I, Kukołowicz P. High accuracy dosimetry with small pieces of Gafchromic films. *Reports of Practical Oncology and Radiotherapy*. 2018;23(2):114-120. doi:10.1016/j.rpor.2018.01.001
15. Wołowiec P, Kukołowicz PF. The analysis of the measurement uncertainty with application of small detectors made of Gafchromic EBT films for the range of doses typical for in vivo dosimetry in teleradiotherapy. *Radiat Meas*. 2016;92:72-79. doi:10.1016/j.radmeas.2016.08.001
16. Aland T, Moylan R, Kairn T, Trapp J. Effect of verification imaging on in vivo dosimetry results using Gafchromic EBT3 film. *Physica Medica*. 2016;32(11):1461-1465. doi:10.1016/j.ejmp.2016.10.020
17. Lewis D, Micke A, Yu X, Chan MF. An efficient protocol for radiochromic film dosimetry combining calibration and measurement in a single scan. *Med Phys*. 2012;39(10):6339-6350. doi:10.1118/1.4754797
18. Micke A, Lewis DF, Yu X. Multichannel film dosimetry with nonuniformity correction. *Med Phys*. 2011;38(5):2523-2534. doi:10.1118/1.3576105
19. Dönmez Kesen N, Köksal Akbaş C. The investigation of the anisotropic analytical algorithm (Aaa) and the acuros xb (axb) dose calculation algorithms accuracy in surface and buildup region for 6 mv photon beam using gafchromic ebt3 film. *Turk Onkoloji Dergisi*. 2021;36(3):365-372. doi:10.5505/tjo.2021.2690
20. Trombetta DM, Cardoso SC, Alves VGL, Facure A, Batista DVS, Da Silva AX. Evaluation of the radiotherapy treatment planning in the presence of a magnetic valve tissue expander. *PLoS One*. 2015;10(2). doi:10.1371/journal.pone.0117548
21. Thompson RCA, Morgan AM. Investigation into dosimetric effect of a MAGNA-SITE™ tissue expander on post-mastectomy radiotherapy. In: *Medical Physics*. Vol 32. John Wiley and Sons Ltd; 2005:1640-1646. doi:10.1118/1.1914545
22. Asena A, Kairn T, Crowe SB, Trapp J V. Establishing the impact of temporary tissue expanders on electron and photon beam dose distributions. *Physica Medica*. 2015;31(3):281-285. doi:10.1016/j.ejmp.2015.01.015
23. Chatzigiannis C, Lymperopoulou G, Sandilos P, et al. Dose perturbation in the radiotherapy of breast cancer patients implanted with the Magna-Site: a Monte Carlo study. *J Appl Clin Med Phys*. 2011;12(2):58-70. doi:10.1120/jacmp.v12i2.3295
24. Damast S, Beal K, Ballangrud Å, et al. Do metallic ports in tissue expanders affect postmastectomy radiation delivery? *Int J Radiat Oncol Biol Phys*. 2006;66(1):305-310. doi:10.1016/j.ijrobp.2006.05.017
25. Park SH, Kim YS, Choi J. Dosimetric analysis of the effects of a temporary tissue expander on the radiotherapy technique. *Radiologia Medica*. 2021;126(3):437-444. doi:10.1007/s11547-020-01297-6
26. Yoon J, Xie Y, Heins D, Zhang R. Modeling of the metallic port in breast tissue expanders for photon radiotherapy. *J Appl Clin Med Phys*. 2018;19(3):205-214. doi:10.1002/acm2.12320
27. Fogliata A, Nicolini G, Vanetti E, Clivio A, Cozzi L. Dosimetric validation of the anisotropic analytical algorithm for photon dose calculation: Fundamental characterization in water. *Phys Med Biol*. 2006;51(6):1421-1438. doi:10.1088/0031-9155/51/6/004
28. Cheng ZJ, Bromley RM, Oborn B, Carolan M, Booth JT. On the accuracy of dose prediction near metal fixation devices for spine SBRT. *J Appl Clin Med Phys*. 2016;17(3):475-485. doi:10.1120/jacmp.v17i3.5536
29. Ojala J, Kapanen M, Sipila¨ P, Hyo¨dynmaa S, Pitka¨nen M. The accuracy of Acuros XB algorithm for radiation beams traversing a metallic hip implant - comparison with measurements and Monte Carlo calculations. *J Appl Clin Med Phys*. 2014;15(5):162-176. doi:10.1120/jacmp.v15i5.4912
30. Pawałowski B, Ryczkowski A, Panek R, Sobocka-Kurdyk U, Graczyk K, Piotrowski T. Accuracy of the doses computed by the Eclipse treatment planning system near and inside metal elements. *Sci Rep*. 2022;12(1). doi:10.1038/s41598-022-10072-8